



Discovery of a Filamentary Synchrotron Structure Connected to the Coherent Magnetic Field in the Outer Galaxy

J. L. West¹, J. L. Campbell^{1,2}, P. Bhaura², R. Kothes³, S. Safi-Harb⁴, J. M. Stil⁵, A. R. Taylor^{6,7,8}, T. Foster⁹, B. M. Gaensler^{1,2}, S. J. George¹⁰, S. J. Gibson¹¹, and R. Ricci^{12,13}

¹Dunlap Institute for Astronomy and Astrophysics, University of Toronto, Toronto, ON, M5S 3H4, Canada; jennifer.west@dunlap.utoronto.ca

²David A. Dunlap Department of Astronomy and Astrophysics, University of Toronto, Toronto, ON, M5S 3H4, Canada

³National Research Council Canada, Herzberg Research Centre for Astronomy and Astrophysics, Dominion Radio Astrophysical Observatory, PO Box 248, Penticton, BC, V2A 6J9, Canada

⁴Department of Physics and Astronomy, University of Manitoba, Winnipeg, MB, R3T 2N2, Canada

⁵Department of Physics and Astronomy, The University of Calgary, 2500 University Drive NW, Calgary, AB, T2N 1N4, Canada

⁶Inter-University Institute for Data Intensive Astronomy, South Africa

⁷University of Cape Town, South Africa

⁸University of the Western Cape, South Africa

⁹Department of Physics and Astronomy, Brandon University, 270-18th Street, Brandon, MB, R7A 6A9, Canada

¹⁰School of Physics and Astronomy, University of Birmingham, Birmingham, B15 2TT, UK

¹¹Department of Physics and Astronomy, Western Kentucky University, Bowling Green, KY 42101, USA

¹²Istituto Nazionale Ricerche Metrologiche—Strada delle Cacce 91, Torino, I-10135, Italy

¹³INAF-Istituto di Radioastronomia, Via Gobetti 101, Bologna, I-40129, Italy

Received 2022 April 5; revised 2022 October 13; accepted 2022 October 15; published 2022 December 7

Abstract

Using data from the Galactic Arecibo *L*-band Feed Array Continuum Transit Survey, we report the discovery of two previously unidentified, very compressed, thin, and straight polarized filaments approximately centered at Galactic coordinates, $(l, b) = (182.5, -4.0)$, which we call G182.5–4.0. Using data from the Isaac Newton Telescope Galactic Plane Survey, we also find straight, long, and extremely thin $H\alpha$ filaments coincident with the radio emission. These filaments are positioned in projection at the edge of the Orion-Eridanus superbubble and we find evidence indicating that the filaments align with the coherent magnetic field of the outer Galaxy. We find a lower limit on the total radio flux at 1.4 GHz to be 0.7 ± 0.3 Jy with an average linearly polarized fraction of $40^{+30}_{-20}\%$. We consider various scenarios that could explain the origin of these filaments, including a shell-type supernova remnant (SNR), a bow shock nebula associated with a pulsar, or relic fragments from one or more supernova explosions in the adjacent superbubble, with a hybrid scenario being most likely. This may represent an example of a new class of objects that is neither an SNR nor a bow shock. The highly compressed nature of these filaments and their alignment with the Galactic plane suggests a scenario where this object formed in a magnetic field that was compressed by the expanding Orion-Eridanus superbubble, suggesting that the object is related to this superbubble and implying a distance of ~ 400 pc.

Unified Astronomy Thesaurus concepts: [Interstellar medium \(847\)](#); [Supernova remnants \(1667\)](#); [Radio continuum emission \(1340\)](#)

1. Introduction

As the resolution and sensitivity of observations improve, we are increasingly finding that the interstellar medium (ISM) of our Galaxy is filled with filamentary (i.e., long and narrow) structures from a variety of different origins. These filaments are observed in emission across the electromagnetic spectrum including with X-rays (e.g., De Vries & Romani 2022), ultraviolet (UV; e.g., Bracco et al. 2020), optical (e.g., Fesen et al. 2021), infrared (e.g., Green et al. 2022), and radio (e.g., Yusef-Zadeh et al. 1984; Heywood et al. 2022), and there are also long and narrow structures detected through non-emitting tracers such as Faraday rotation (e.g., Campbell et al. 2022) and scintillation of background sources (e.g., Wang et al. 2021). The filaments are associated with many different environments and origins including star-forming regions, supernova remnants (SNRs), bow shock nebulae, and also filaments of uncertain

origins (e.g., Jelić et al. 2015; Bracco et al. 2020), and the radiation can come from both thermal and nonthermal (i.e., synchrotron) emission mechanisms.

There is also evidence that the orientation of filaments are connected to magnetic fields (Clark et al. 2014; Jelić et al. 2015; Zaroubi et al. 2015; Planck Collaboration et al. 2016; West et al. 2021; Campbell et al. 2022). Spiral galaxies, including the Milky Way, are known to have coherent large (galactic)-scale magnetic fields (Beck 2015), which are thought to originate through the $\alpha - \Omega$ dynamo and compression from spiral shocks and supernova (SN) explosions (Beck 2015). Outflows, perhaps from superbubbles, driven by SNe are needed to drive the dynamo process (Parker 1992).

There is strong evidence that the shells of SNRs align with the large-scale, mean Galactic magnetic field on scales $\gtrsim 10$ pc (Caswell 1977; Gaensler 1998; West et al. 2016). The blast wave of the SN compresses the ambient medium, freezing in the magnetic field. As the SNR ages, it is thought to become stretched out and elongated parallel to the magnetic field. The timeline depends strongly on the magnetic tension and therefore the magnetic field strength. In the Galactic center, there are many straight and compressed nonthermal filaments



Original content from this work may be used under the terms of the [Creative Commons Attribution 4.0 licence](#). Any further distribution of this work must maintain attribution to the author(s) and the title of the work, journal citation and DOI.

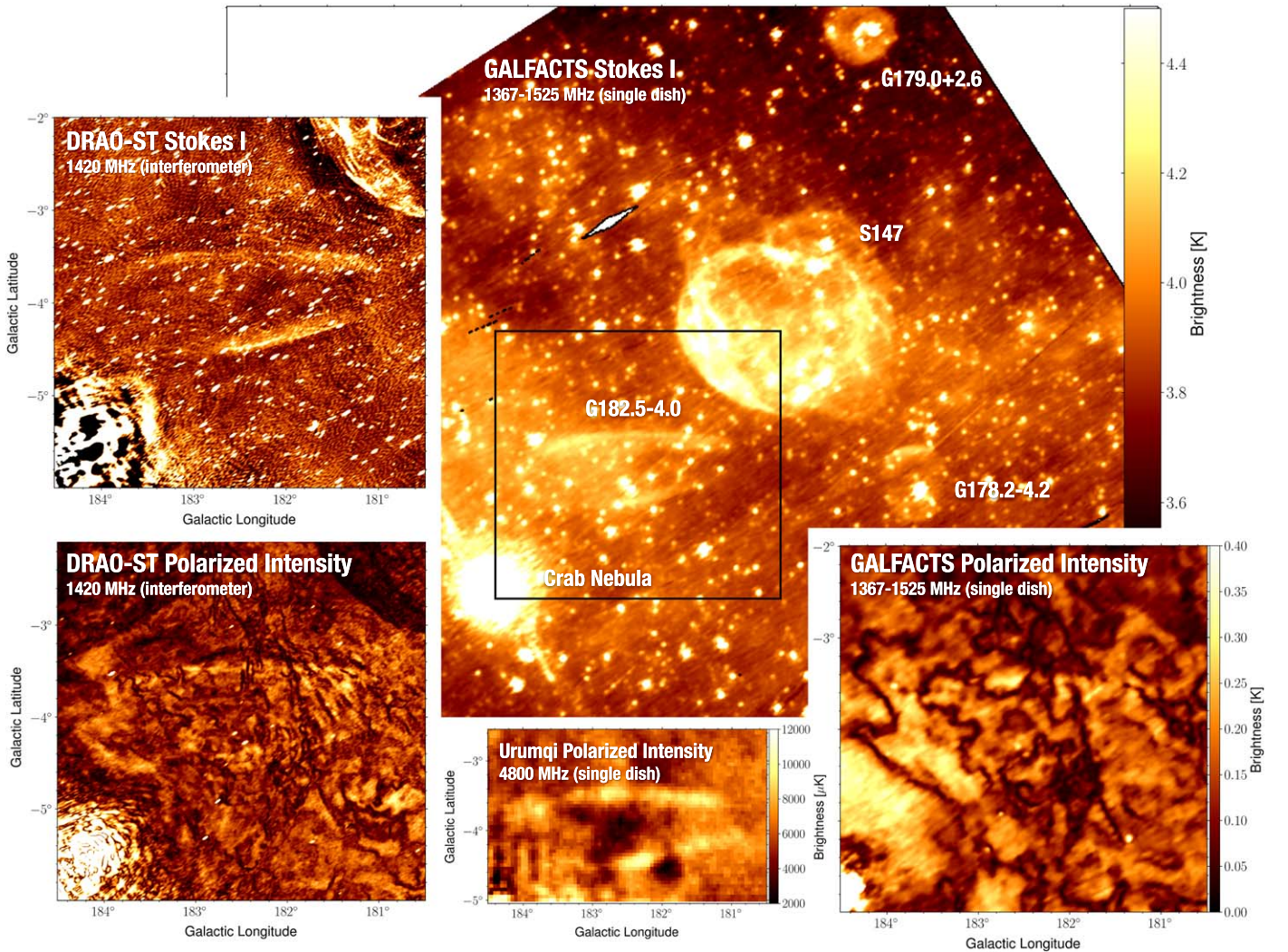


Figure 1. G182.5 and surrounding area for the GALFACTS Stokes I (main image), DRAO-ST Stokes I (top left inset), DRAO-ST polarized intensity (bottom left inset), Urumqi polarized intensity data (bottom center inset), and GALFACTS peak polarized intensity data (bottom-right inset). The black square in the main image indicates the region shown in the inset images. Prominent features in the surrounding area are labeled.

(Yusef-Zadeh et al. 1984; Heywood et al. 2022) that are thought to possibly be relics of old SNRs (Sofue 2020). There is also increasing evidence that the neutral hydrogen (H I) component of the Galaxy contains filamentary structures, or “fibres,” that align with the Galactic magnetic field (Clark et al. 2014).

We have discovered two previously unidentified, faint, radio-synchrotron-emitting filaments located toward the outer Galaxy, shown in Figure 1. We assume that these filaments have the same origin, and thus we consider them to be part of a single structure, which we call G182.5–4.0. The filaments are located at the edge of the Orion-Eridanus superbubble (distance ≈ 400 pc; Ochsendorf et al. 2015), as shown in Figure 2. The structure shares similarities both with known SNRs and bow shock nebulae, but yet it does not conform to the typical properties of either of these classes of object.

Radio observations of nonthermal synchrotron radiation implies the existence of relativistic electrons in a magnetic field. This radiation is intrinsically polarized with a negative spectral index, $\alpha < 0$ (where the flux density $S_\nu \propto \nu^\alpha$), which distinguishes it from thermal bremsstrahlung radiation that can also be bright at radio frequencies. Radio synchrotron

brightness is proportional to the plane-of-sky magnetic field component, B_\perp . Polarized radiation also undergoes Faraday rotation, the study of which reveals additional information about the line-of-sight (LOS) magnetic field strength (B_\parallel) and direction.

An electromagnetic wave undergoes Faraday rotation as it propagates through a magneto-ionic medium. The Faraday depth, $\phi(d)$, is defined as the integral of the magneto-ionic medium along a LOS, from a distance, $r = d$, to the observer at $r = 0$:

$$\phi(d) = 0.812 \int_0^d n_e B_\parallel dr [\text{rad m}^{-2}]. \quad (1)$$

Here n_e (in units of cm^{-3}) is the thermal electron density and $B_\parallel > 0$ (in units of μG) when the magnetic field is pointed toward the observer.

In the simplest observational case, $\phi(d)$ can be found by measuring the dependence of the position angle of the polarization vector, χ , as a function of λ^2 (in units of m^2). When the total Faraday depth of a background source is measured through a Faraday-rotating medium, then we call this

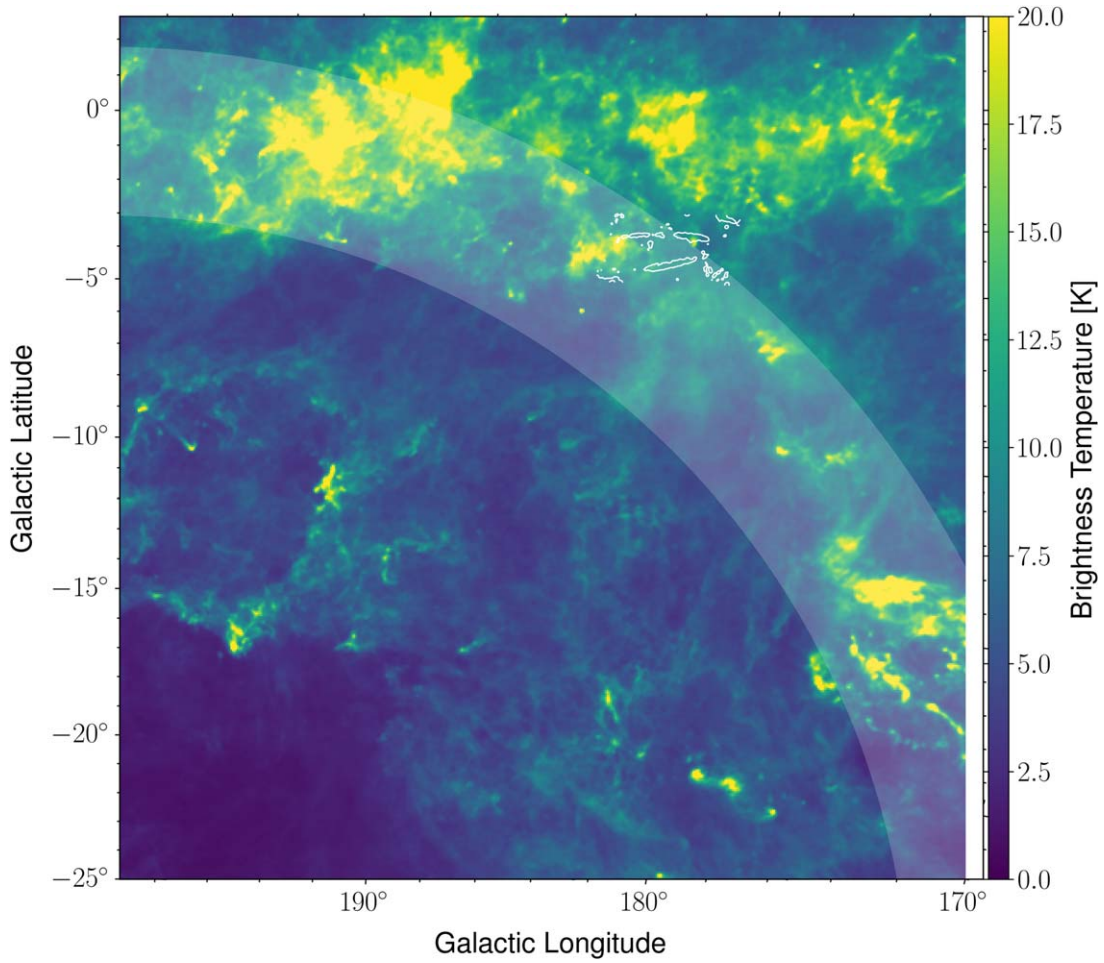


Figure 2. Planck 545 GHz dust image showing a portion of the Orion-Eridanus superbubble. The approximate edge of the bubble is shown by the shaded white band (based on Ochsendorf et al. 2015 and Tahani et al. 2022). The white contours near the top right are the DRAO Stokes I data showing the position and orientation of the G182.5–4.0 filaments.

the Faraday rotation measure, RM, where

$$\chi_{\text{obs}} = \chi_{\text{src}} + \text{RM}\lambda^2. \quad (2)$$

The amount of rotation (i.e., the difference between χ_{obs} and χ_{src}) is $\propto \lambda^2$, and thus can be significantly greater at longer wavelengths.

In the case of diffuse synchrotron emission, where there is both rotation and emission along the same LOS, the amount of rotation (and thus the Faraday depth) will vary for each point along the LOS where the emission is taking place. Here, the simple linear relationship between χ and λ^2 no longer holds and instead we use the technique of RM synthesis (Brentjens & de Bruyn 2005) to measure the polarized intensity as a function of Faraday depth, where

$$\mathbf{F}(\phi) = \int_{-\infty}^{\infty} \mathbf{P}(\lambda^2) e^{-2i\phi\lambda^2} d\lambda^2. \quad (3)$$

Here, $\mathbf{P}(\lambda^2) = Q(\lambda^2) + iU(\lambda^2)$ is the linearly polarized intensity, where Q and U are the linear polarization Stokes parameters and $\mathbf{F}(\phi)$ is the polarized intensity as a function of Faraday depth. From this process, we measure a Faraday depth spectrum. The simplest analysis measures the peak of this spectrum, ϕ_{peak} , which tells us the average Faraday depth integrated along the LOS.

In this paper, we explore the properties of G182.5–4.0 and its possible connection to the large-scale Galactic magnetic field with the goal of understanding its origin. In Section 2 we describe the data that we use to measure the structure’s properties, which are presented in Section 3. We present a radial profile (Section 3.1) and look for evidence connecting these filaments to the large-scale Galactic field using starlight polarization (Section 3.2), neutral hydrogen structures (Section 3.3), and Faraday rotation (Section 3.4). Discussion and conclusions are presented in Sections 4 and 5, respectively.

2. Observations

2.1. Arecibo

G182.5–4.0 consists of two straight and nearly parallel filaments, first identified in data from the Galactic Arecibo L -band Feed Array Continuum Transit Survey (GALFACTS) using the 305 m Arecibo radio telescope (data release version 3.1.2). These data have full Stokes polarization (I , Q , U , and V) observed over 1367–1525 MHz, with a channel width of 0.42 MHz (Taylor & Salter 2010). These data have a beam FWHM ≈ 3.5 and a band-averaged sensitivity of $90 \mu\text{Jy beam}^{-1}$. In Figure 1 we show the total intensity and peak polarized intensity, $\mathbf{F}(\phi_{\text{peak}})$, maps for these data (see Section 3.4 for further details).

2.2. Dominion Radio Astrophysical Observatory Synthesis Telescope

We obtained observations using the Dominion Radio Astrophysical Observatory Synthesis Telescope (DRAO-ST; Landecker et al. 2000) with continuum observations at 1.4 GHz in Stokes I , Q , and U , in addition to HI spectral line observations. The main characteristics of this survey are the same as for the Canadian Galactic Plane Survey (Taylor et al. 2003). As we are mapping close to one of the brightest radio sources in the sky, the Crab Nebula, we placed the three fields covering G182.4–4.0 so that the Crab Nebula was in the first null of the antenna’s primary beam at 1420 MHz, in order to reduce artifacts.

The spectral line observations cover a velocity range of 256 channels from 85.1 to -125.1 km s^{-1} with a channel width of 0.825 km s^{-1} . The angular resolution varies slightly across the maps as $\text{cosec}(\text{decl.})$. At the center of G182.5–4.0 the resolution is $125'' \times 49''$ at 1420 MHz in Stokes I and $134'' \times 59''$ in the HI line and in the linear polarization data. The rms noise is about 20 mK or $200 \mu\text{Jy beam}^{-1}$ in the continuum images and about 1 K per 0.825 km s^{-1} channel for the HI data. These data do not have short spacings added and therefore they are missing the zero level flux.

2.3. Urumqi

We also use higher-frequency (4800 MHz) but lower-resolution data ($\text{FWHM} = 9.5$) from the Urumqi 25 m telescope (Gao et al. 2010).¹⁴ The relatively high frequency means that the Faraday rotation is negligible for these data, making them useful to derive the polarized fraction. These data are absolute-level corrected with extrapolated Wilkinson Microwave Anisotropy Probe K -band data in International Astronomical Union convention from the 9 yr release.

2.4. Other Data

We use the combined $\text{H}\alpha$ data from the Virginia Tech Spectral line Survey and the Wisconsin $\text{H}\alpha$ Mapper (WHAM; Haffner et al. 2003, $\text{FWHM} = 6'$),¹⁵ to look for diffuse ionized gas around G182.5–4.0.

In addition, we use the high-resolution ($\text{FWHM} \sim 1''$) Isaac Newton Telescope Galactic Plane Survey (IGAPS) to search $\text{H}\alpha$, UV, and other optical data (g , r , and i filters).¹⁶ We identify multiple long ($>0.5^\circ$), thin ($<0.0015^\circ$) counterparts, and a straight $\text{H}\alpha$ counterpart to the radio filaments in both the north and the south, shown in Figure 3. There is no evidence for these filaments in the other filters, including UV. Other authors (Bracco et al. 2020; Fesen et al. 2021) have detected thin filaments with $\text{H}\alpha$ counterparts in far-UV (FUV) using the Galaxy Explorer All Sky Survey (GALEX) data. Unfortunately, FUV GALEX data for the region around G182.5–4.0 are not available so we are unable to check for the presence of these filaments in that filter.

We also use archival data of thermal dust emission from Planck at 545 GHz¹⁷ in order to compare the position of G182.5–4.0 to the wall of the Orion-Eridanus shell.

3. Observed Properties

The two radio filaments are approximately 2.7 and 1.7 degrees long, with a separation that varies from about 0.5 on the western side to 1.0 on the eastern side (see Figure 1). They are oriented roughly parallel to the Galactic plane, with a by-eye orientation of $89^\circ \pm 3^\circ$ (northern filament), and $104^\circ \pm 3^\circ$ (southern filament), where 90° is parallel to the Galactic plane. They have an approximate geometric center point at $(l, b) = (182.5, -4.0)$. In the brightest region in the south, the surface brightness is only about 0.2 K above the background level.

We detect long and thin $\text{H}\alpha$ filaments coincident with the radio emission (see Figure 3) with an aspect ratio of $\approx 500:1$. The southern $\text{H}\alpha$ filament is detected across about 0.5 of sky with a width of only $\sim 4''$. They are also very faint, being only $1-2\sigma$ above the noise limit of the data, which has a magnitude limit of 21 mag (Drew et al. 2005). Using the IPHAS flux conversion from Barentsen et al. (2014, in-band $\text{H}\alpha$ flux for Vega is $1.52 \times 10^{-7} \text{ erg cm}^{-2} \text{ s}^{-1}$), we find that the filaments have an approximate surface brightness of 1–3 Rayleighs (R) (where $1 \text{ R} = 5.661 \times 10^{-18} \text{ erg s}^{-1} \text{ cm}^{-2} \text{ arcsec}^{-2}$ for $\text{H}\alpha$). This is somewhat brighter than the $\text{H}\alpha$ counterpart to the 30° long UV filament detected by Bracco et al. (2020), where the brightness was $\approx 0.5 \text{ R}$. Our values are consistent with the brightnesses of evolved SNR filaments found by Fesen et al. (2021).

Due to uncertainty in the zero point of the GALFACTS map, we use the DRAO Stokes I map to estimate the flux density. We first remove the point sources by fitting and subtracting elliptical Gaussians to the unresolved sources. The SNR flux density is then found by taking the sum in a rectangular box measuring 2.75 by 1.2 centered on $(l, b) = (182.3, -4.0)$. We estimate a constant background level and its uncertainty by finding the average and standard deviation of ten 0.5 square regions in the region around the main box. We find a flux density $S_{1.4 \text{ GHz}} = 0.7 \pm 0.3 \text{ Jy}$. However, since the DRAO map is missing flux from the absence of zero spacings, we note that this is only a lower limit on the flux density.

From the DRAO polarized intensity ($P = \sqrt{Q^2 + U^2}$) image (bottom left of Figure 1), the filaments are distinctly visible. Polarized synchrotron emission has a theoretical maximum polarized fraction of about 70%. Observed polarized fraction values are rarely this high due to various depolarizing effects. Depolarization occurs due to changes in the orientation of the polarization pseudo-vector along the LOS (depth depolarization), within the beam of the telescope (beam depolarization), and across the bandwidth of the observation (bandwidth depolarization). The large GALFACTS beam causes significant beam depolarization in the polarized intensity image (bottom right of Figure 1), making the filaments difficult to see.

Both depth and beam depolarization can occur due to random (turbulent) fluctuations, and they will have much less impact in a highly ordered magnetic field. Faraday rotation can further scramble the polarization pseudo-vectors, enhancing the depolarizing effects of all three mechanisms. In order to decouple the depolarizing effects of Faraday rotation and turbulence, we measure the polarization fraction, $p = P/I$, at high frequencies where the Faraday rotation is negligible. Therefore we use the higher-frequency data from the Urumqi telescope (shown in Figure 1), which avoids the depolarizing effects of Faraday rotation that impacts the lower-frequency DRAO and GALFACTS data. We use the higher-resolution

¹⁴ Data obtained from <https://www3.mpifr-bonn.mpg.de/survey.html>.

¹⁵ Data obtained from SkyView, <http://skyview.gsfc.nasa.gov>.

¹⁶ Data obtained from <https://www.igapsimages.org>.

¹⁷ Data obtained from SkyView, <http://skyview.gsfc.nasa.gov>.

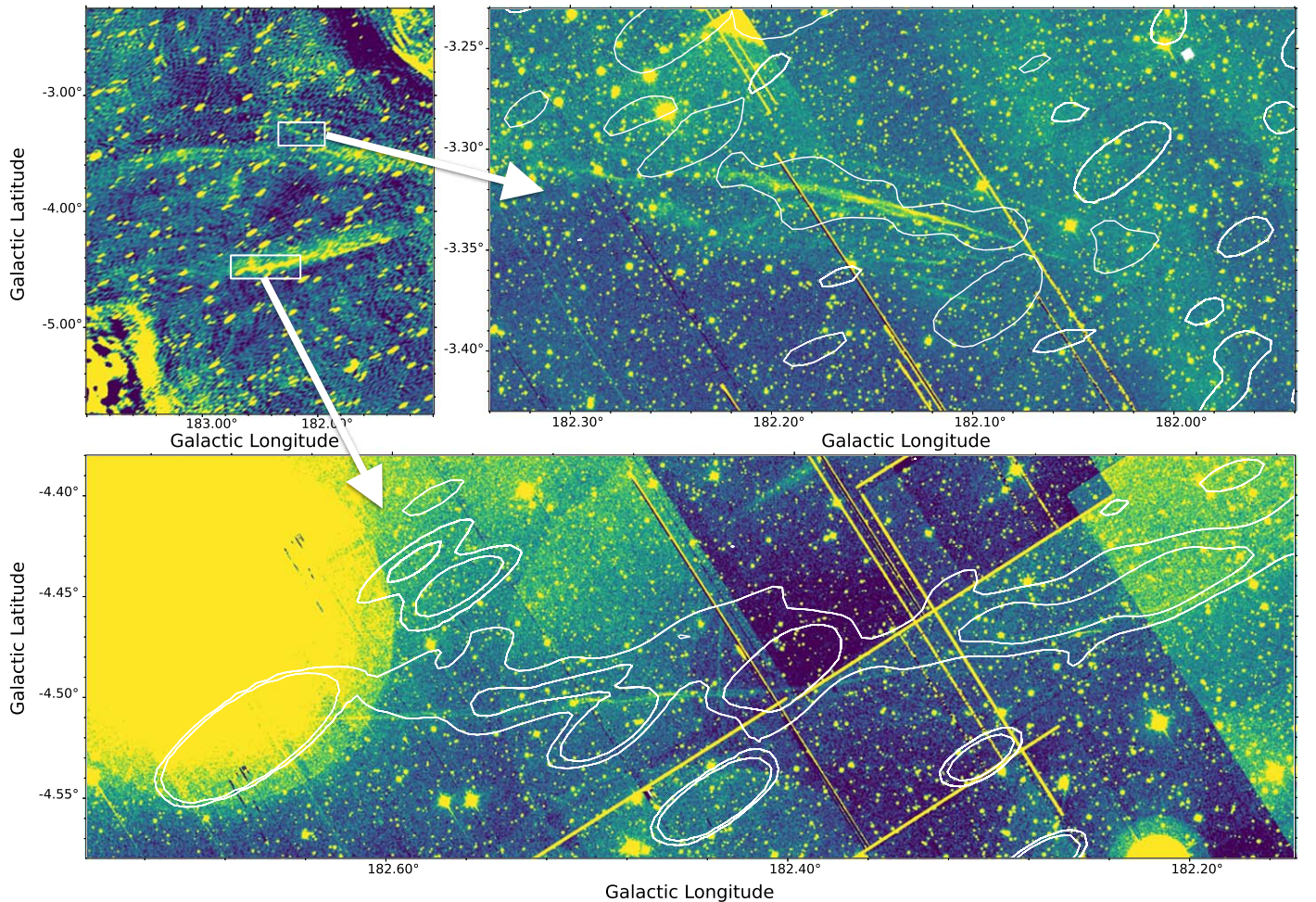


Figure 3. $H\alpha$ filaments detected in the IGAPS data with contours from Stokes I . The DRAO Stokes I image is shown at upper left with white rectangles indicating the regions shown in the $H\alpha$ mosaics. In all panels, yellow shows bright emission and dark blue shows faint.

DRAO image as a guide to avoid measuring areas contaminated by bright compact sources. We first subtract the average background level, and then measure the mean Stokes I , Q , and U in small ($28.5' \times 9.5'$) regions on the brightest regions of the northern and southern filaments. The bias-corrected polarized intensity is found by $P = \sqrt{Q^2 + U^2 - (1.2\sigma_{QU})^2}$, where $\sigma_{QU} = 800 \mu\text{K}$. In both filaments, we measure similarly high polarized fractions of $p = 40\%_{-20\%}^{+30\%}$. The high uncertainty is due to the large variability in the background level. The presence of coincident $H\alpha$ filaments indicates that some small amount of the Stokes I flux is from thermal bremsstrahlung radiation. This would decrease the component of Stokes I coming from the synchrotron radiation, making the measured polarized fraction a lower limit. Despite these being a lower limit, this is a very high polarized fraction value, indicating the presence of a very compressed and highly coherent magnetic field that is not dominated by turbulence.

3.1. Synchrotron Radial Profile

A strong shock, such as that from a SN explosion, forms a compressed shell that can be characterized with a Sedov–Taylor mass density profile (Sedov 1959), which gives the observed shell a characteristic brightness profile. This profile has a shallower slope on the interior of the shock and a steeper

slope at the outer shock boundary. Using the DRAO Stokes I data, we make an averaged profile across the northern and southern filaments to check if the profile is consistent with the two filaments being on either side of an interior explosion (i.e., the shock travels from a point in the center outwards) or whether the shock has impacted both filaments from the same direction, as we would expect if the filaments were both located on the same edge of a much larger shell.

We define two boxes with each filament running through the center. For the northern filament, the box is $2^\circ 0' \times 1^\circ 0'$, extending from $181.4 < l < 183.4$ and $-4.0 < b < -3.0$. For the southern filament, the image is first rotated by 13° so that the box can be defined approximately perpendicular to the filament. This box extends $1^\circ 5' \times 1^\circ 0'$ from approximately $181.2 < l < 182.7$ and $-5.0 < b < -4.0$. The values are averaged along the long dimension of the box (longitude axis) and then plotted along the short dimension of the box (latitude axis). In the top panel of Figure 4, it is clear that the profiles of the northern and the southern filaments have an opposite shape, indicating that the steeper slope is located at the outer edge of each filament. This is consistent with the origin of the shock being centrally located between the two filaments. Here the angular dimension is converted to a physical scale using an assumed distance of 400 pc.

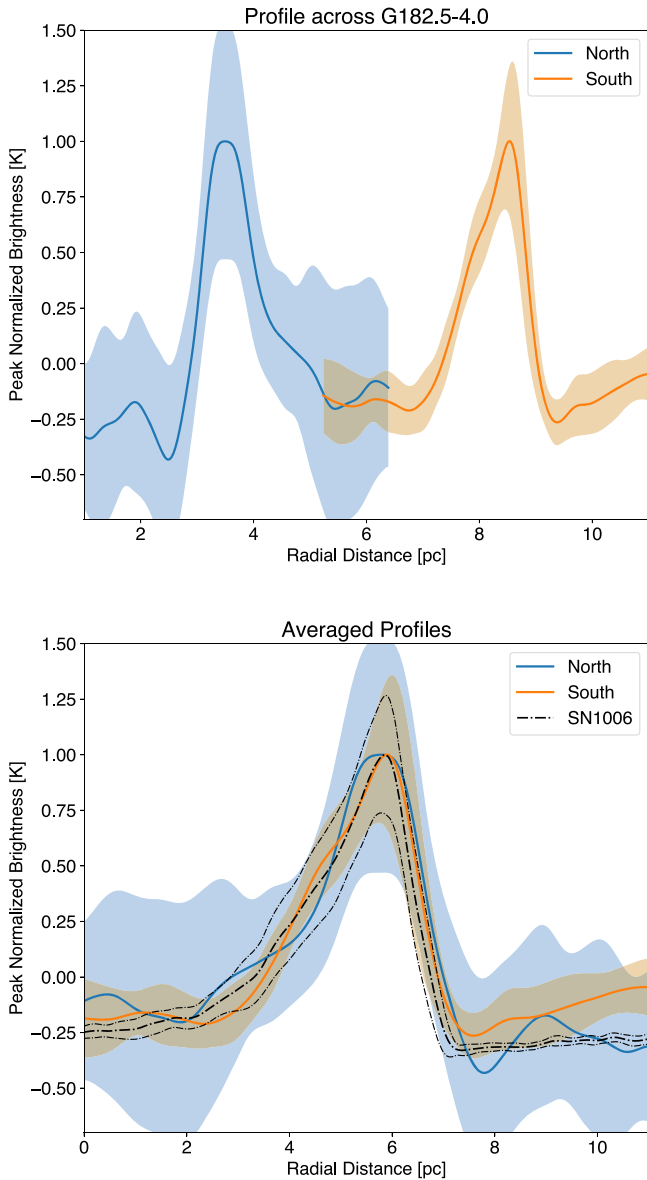


Figure 4. Top: Profile across both the northern and southern filaments of G182.5–4.0. The peak brightness has been normalized to 1. The shading shows the 1σ uncertainty on the average. Bottom: Profile across both the northern and southern filaments of G182.5–4.0 shown in comparison to the profile of the eastern limb of SN1006. Here the northern filament profile has been flipped such that the center of the shell is at a distance of 0 pc. The peak brightness has been normalized to 1. As in the top panel, the shading (upper and lower dashed lines in the case of SN1006) shows the 1σ uncertainty on the average.

We also compare the profiles to that from a canonical SNR, SN1006. Using archival 843 MHz data from the Sydney University Molonglo Sky Survey¹⁸ we make a similar profile of the eastern limb of SN1006 averaging over a box measuring $0^{\circ}.2$ in latitude and $0^{\circ}.4$ in longitude. Assuming a distance to SN1006 of 1.85 kpc (Green 2019, and references therein), we find that the physical scale is approximately double that of G182.5–4.0. Thus, in order to show the profiles on the same scale, for the bottom panel of Figure 4 we use a distance of 800 pc to convert the angular dimension to a comparable physical scale (instead of 400 pc used in the top panel of

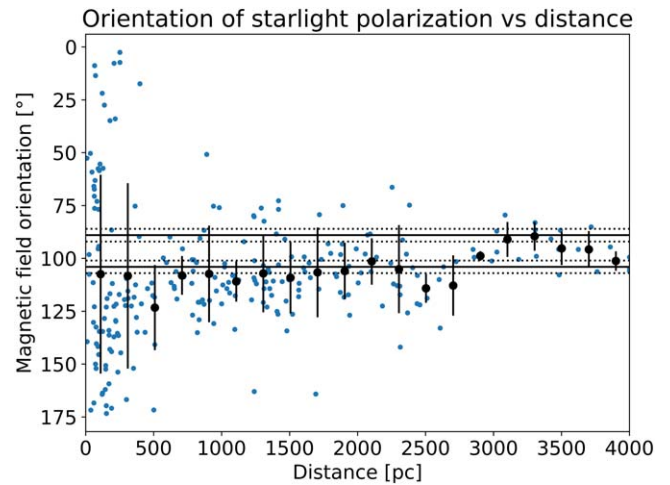


Figure 5. Plot of the orientation angle vs. distance for stars in the catalog of Meng & Sun (2021). The horizontal lines represent the orientation of the two parts of G182.5–4.0 with uncertainty (dotted lines). The black points show the mean and standard deviation of the orientation angles using 200 pc bins.

Figure 4). Since the shape of the Sedov–Taylor profile is self-similar, the physical scaling is somewhat arbitrary and does not impact the comparison of the relative shape of the profile. The profiles are nearly identical, supporting the interpretation that the origin of these filaments are from a shock with a centrally located origin such as that from a SN explosion.

3.2. Polarized Star Catalog

Meng & Sun (2021) cross-matched the Gaia Data Release 2 (DR2) catalog with the starlight polarization catalog from Heiles (2000) to obtain precise distance measurements together with polarization information for 7613 stars. The polarized orientation of a particular star probes the integrated orientation of the magnetic field along the LOS to the star, weighted by the dust mass. In Figure 5, we plot the magnetic field orientation versus distance for a region surrounding G182.5–4.0, between $-10^{\circ} < b < 5^{\circ}$ and $160^{\circ} < l < 200^{\circ}$.

For very nearby stars ($\lesssim 300$ pc), there is a large range of orientations, but between 500 pc and 2.5 kpc the angles are fairly consistent. At relatively large distances ($\gtrsim 2.5$ kpc), there is a small but noticeable shift in the orientation of the starlight polarization. The filament orientations are consistent with a large range of distances, so it is not possible to constrain the distance with this measurement. However it does suggest that either the dust polarization is dominated by a foreground structure, such as the Local Bubble wall and/or the wall of the Orion-Eridinaus superbubble, or that there is a remarkably coherent magnetic field in this direction. In both scenarios, given the similar orientation of the filaments with the dust, it suggests the orientation of the filaments are influenced by the ambient Galactic magnetic field. The former scenario supports an association with the Orion-Eridinaus superbubble wall. Although, even though the magnetic field traced by starlight (i.e., dust) polarization is rather uniform along the LOS, it is difficult to make a strong conclusion about the magnetic field traced by the synchrotron emission because synchrotron and dust have different weightings of the field along the LOS.

¹⁸ Data obtained from SkyView, <https://skyview.gsfc.nasa.gov>.

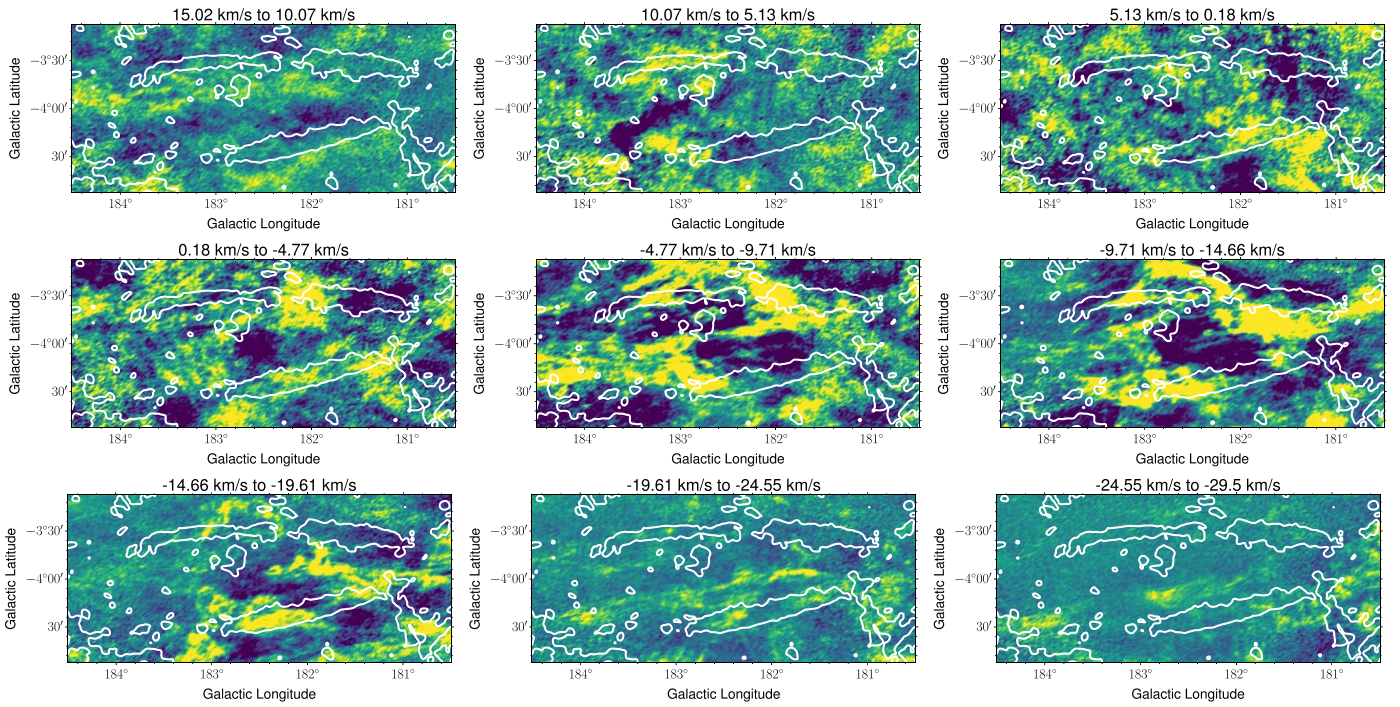


Figure 6. H I velocity maps showing a range of velocities from 15.02 to -28.67 km s^{-1} . Each subplot has been averaged over six velocity channels, showing a total range of 4.95 km s^{-1} . Each map is shown with the same linear brightness scaling from -0.12 (dark blue) to 0.12 K (yellow). The white contours show the position of the Stokes I emission of G182.5–4.0.

3.3. Neutral Hydrogen

In Figure 6 we show a range of the H I spectral channels at velocities from $+15.02$ to -29.5 km s^{-1} , noting that Joubaud et al. (2019) find that the velocities of the H I lines associated with the Orion-Eridanus superbubble range from $+18$ to -15 km s^{-1} . Each subplot has been averaged over a velocity range of 4.95 km s^{-1} , and includes Stokes I contours that show the position of the filamentary structure of G182.5–4.0. A visual inspection of these plots indicates that for some velocities there is evidence of elongated H I structures that appear parallel to the Stokes I filamentary emission. That is, there is a similarity in the orientation of the structures but they are not colocated. The most prominent H I filament is located between the synchrotron filaments, as particularly visible in the center panel of Figure 6 (velocities of -4.77 to -9.71 km s^{-1}), but also to lesser extent at some other velocities (e.g., -19.61 to -24.55 km s^{-1}).

The rolling Hough transform (RHT), an algorithm that quantifies the linearity and spatial coherence of structures in images, has been applied to measure the orientation of linear structures in H I data (Clark et al. 2014). We apply the RHT to both the H I velocity cube and DRAO 1.4 GHz Stokes I data. The RHT uses two parameters, a window length (WLEN) and a smoothing radius (SMR). These parameters control the scale (width and length, respectively) of the filamentary structures that are quantified by the RHT. We use $\text{WLEN} = 0.5$ (101 pixels) and $\text{SMR} = 0.055$ (11 pixels). These values approximately correspond to the width and separation of the synchrotron filaments.

In Figure 7, we show the average orientations of H I and Stokes I structures over a region from $180.75 < l < 184.00$ and $-3.33 > b > -4.50$. The range of angles from the Stokes I image, shown in black, has two closely spaced peaks at 105.7

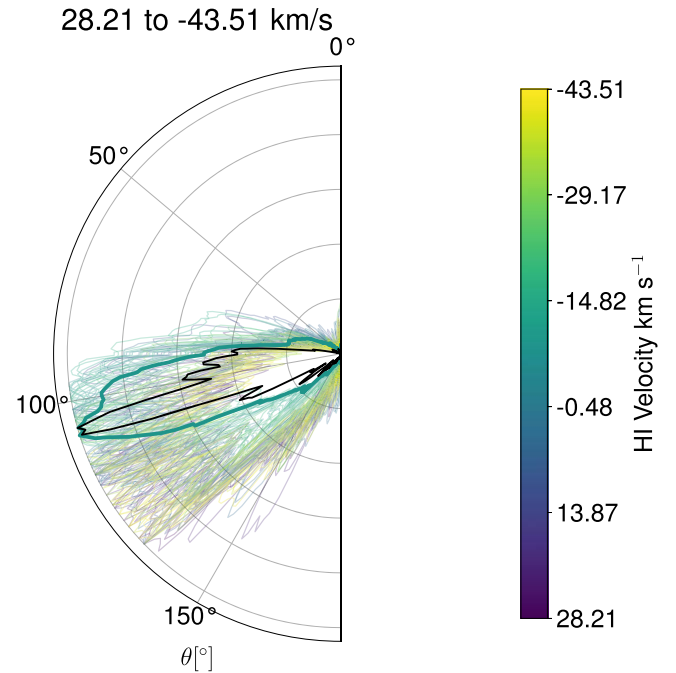


Figure 7. The distribution of RHT orientation angles of H I structures, measured from Galactic north through east, for velocities from 28.21 to -43.51 km s^{-1} . Each curve is an integration over all of the pixels enclosed in a region from $180.75 < l < 184.00$ and $-3.33 > b > -4.50$, and for a particular velocity channel. The black curve shows the result from the Stokes I image. The thicker cyan curve is for an H I velocity channel at $-8.8880 \text{ km s}^{-1}$, which shows the greatest agreement with Stokes I .

and 107.4 , with lesser peaks at 89° , 94° , and 99° . Figure 7 also shows a selection of Galactic H I velocities from 28.21 to -43.51 km s^{-1} . The channel at $-8.8880 \text{ km s}^{-1}$ has peaks that

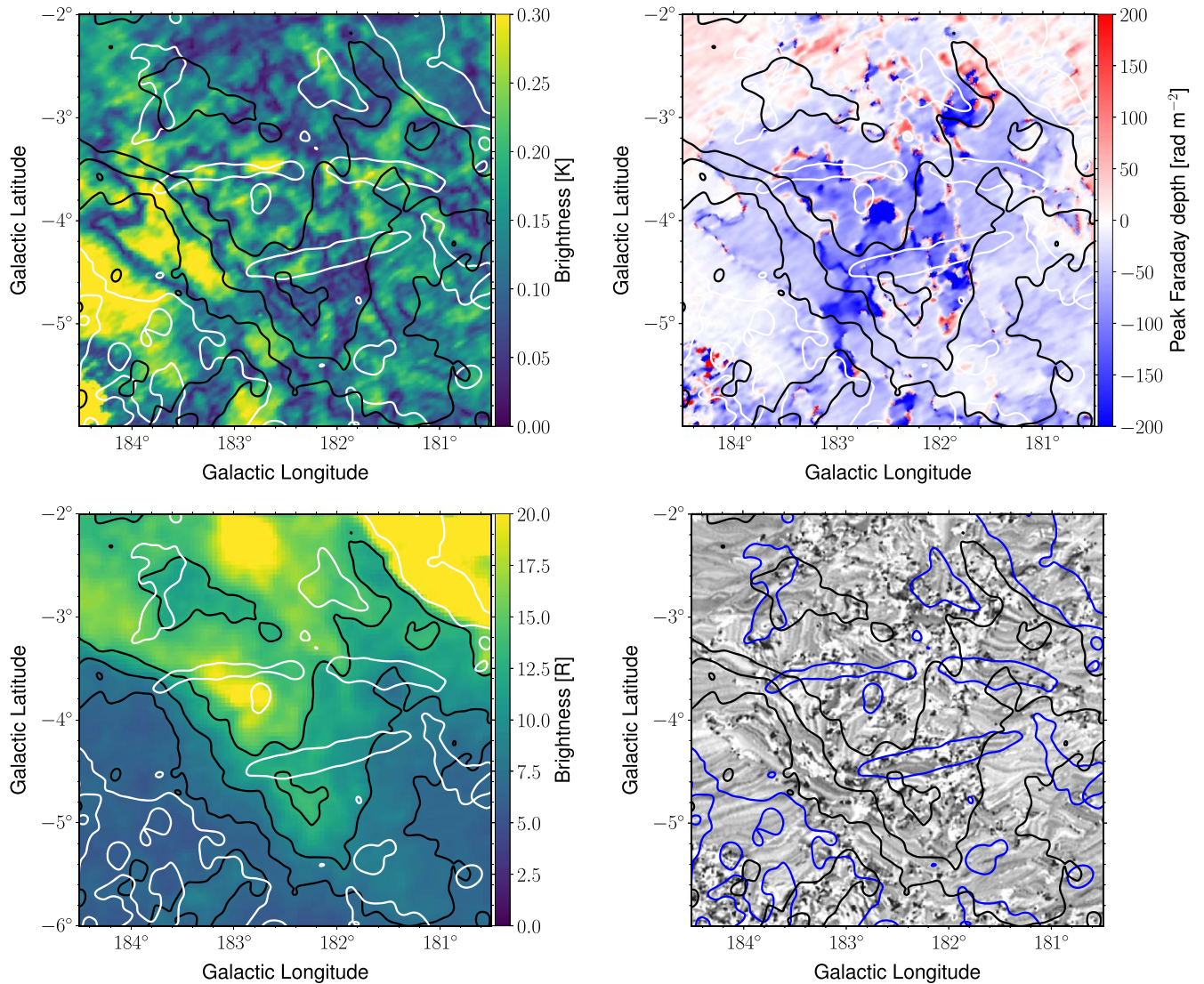


Figure 8. Top left: Map of the peak polarized intensity, $F(\phi_{\text{peak}})$, from GALFACTS. Top right: Map of peak Faraday depth, ϕ_{peak} . Bottom left: WHAM H α map toward the region around G182.5–4.0. Bottom right: LIC drapery lines showing the plane-of-sky magnetic field orientation ($\chi_{\text{src}} + 90^\circ$). All panels have black contours that show the H α emission at levels of 7, 9, and 13 Rayleighs (R). The white contours (blue in the bottom-right panel) are from the DRAO Stokes I data with a level of 0.015 K, showing the position and orientation of the G182.5–4.0 filaments.

are exactly identical to those in Stokes I , and is also consistent with the by-eye measurements from Section 3. Since the orientation of the HI structures are aligned with the synchrotron filaments, it suggests that either they have the same origin or that they are simply both tracing the ambient Galactic magnetic field.

3.4. Rotation Measure Synthesis

We use the RM-Tools package (Purcell et al. 2020) to perform three-dimensional (3D) RM synthesis on the GALFACTS data. For each pixel, we find the peak Faraday depth, ϕ_{peak} , the peak polarized intensity, $F(\phi_{\text{peak}})$, and the polarization angle at the source (i.e., the derotated polarization angle), χ_{src} , which are standard outputs of RM-Tools. The angle is derotated according to Equation (2) using $\text{RM} = F(\phi_{\text{peak}})$ and where λ is a reference frequency, which RM-Tools defines as the central wavelength over the band. Figure 8 shows a map of $F(\phi_{\text{peak}})$ (upper left) and ϕ_{peak} (upper right), and the magnetic

field lines ($\chi_{\text{src}} + 90^\circ$) visualized using the line integral convolution (LIC) technique (lower right; Cabral & Leedom 1993).

ϕ_{peak} is largest in the vicinity of G182.5–4.0, up to a maximum magnitude $\phi_{\text{peak}} \sim -300 \text{ rad m}^{-2}$. Elsewhere the magnitude is largely close to zero. χ_{src} is quite variable and we see obvious depolarization in $F(\phi_{\text{peak}})$ (dark regions), where ϕ_{peak} is high, noted by the rapidly varying pattern in the magnetic field lines. Where ϕ_{peak} is small, the angles are mostly smooth.

In Figure 8 (lower left), we show the diffuse H α emission, which is proportional to the square of the electron density integrated over the path length (i.e., emission measure), and see that some of its highest values are where ϕ_{peak} is also high, and the contours follow the dark regions in the $F(\phi_{\text{peak}})$ map. Since Faraday rotation is proportional to the integrated product of the LOS magnetic field and electron density, the larger values of ϕ_{peak} are more likely due to an increased electron density rather than increased LOS magnetic field strength, although both may

contribute.¹⁹ The coherent magnetic field lines (for example, seen in the region around $(l, b) = (184^\circ, -5^\circ)$), have a similar orientation on either side of the $H\alpha$ emission, implying that the magnetic field may also be coherent in the vicinity of G182.5–4.0. These lines are oriented at $105^\circ \pm 5^\circ$, which is similar to the orientation of the G182.5–4.0 filaments. $\phi_{\text{peak}} < 0$ indicates that the net component of the magnetic field is directed away from the observer.

4. Discussion

G182.5–4.0 is located almost directly toward the Galactic anticenter. Given the Sun’s position at 8.15 ± 0.15 kpc from the Galactic center (Reid et al. 2019), this implies that, in this direction, we are looking through a reasonably small path length through to the edge of the Galaxy. Current Galactic magnetic field models (e.g., Page et al. 2007; Sun et al. 2008; Jaffe et al. 2010; Jansson & Farrar 2012) agree that in this direction the mean magnetic field should be oriented both almost entirely parallel to the Galactic plane, and such that it is in the plane of the sky with little component directed toward or away from the Sun.

By the same argument, the rotation of the Galaxy in this direction is expected to be almost entirely perpendicular to the LOS. Thus, any structures seen at particular HI velocities in this direction are expected to be dominated by peculiar velocities, and not due to Galactic rotation (Burton 1972; Foster & Cooper 2010). For the specific location of G182.5–4.0, we also see HI at a broad range of velocities due to the superposition and/or association with the edge of the expanding Orion-Eridanus superbubble (Joubaud et al. 2019).

Our analysis shows a clear correspondence between the orientation of Stokes I radio filaments, starlight polarization from dust, and HI fibers. The presence of polarized emission indicates the synchrotron filaments must be magnetic in nature. We consider several options to explain their origin.

4.1. An old SNR?

G182.5–4.0 could be a SNR given that these are the most common polarized, shell-type objects that can be seen at radio wavelengths. SNRs in the radiative phase are typically optically bright and sources of thermal electrons, which cause depolarization. The old SNR S147 is a typical example. It can be seen in Figure 1, located to the northeast of G182.5–4.0, as highly depolarized with a sharp edge. The polarized radio emission with coincident $H\alpha$ emission that we observe in G182.5–4.0 supports the old SNR hypothesis. Our analysis of the shape of the radial profile in Section 3.1 shows that it has a nearly identical shape to the known SNR SN1006. This further supports the SNR interpretation.

However, G182.5–4.0 still has a very unusual morphology for an SNR, which are typically round and have a closed geometry (i.e., like two halves of a bubble). In contrast, these filaments are very elongated, and appear to converge only on one end, with only a slight indication that the other end might also curve inwards. Where optical emission is observed in other

SNRs, it is usually a complex network of filaments in the shell rather than the isolated strands seen in G182.5–4.0. There are some known SNRs that have somewhat similar morphology, like G065.1+00.6 (Landecker et al. 1990) and G296.5+10.0 (Dickel & Milne 1976), although these still lack the straight edges and open morphology seen in G182.5–4.0.

The filaments of G182.5–4.0 appear very thin and straight, and are highly polarized, which implies high compression and therefore a highly evolved age. The location of G182.5–4.0 near the edge of the Orion-Eridanus superbubble, as shown in Figure 2, suggests a possible association. A superbubble is not created by a single explosion, but rather the combined effects of winds and SNe in different locations within the bubble. Thus, its shape is not expected to be uniformly spherical, and the shaded band in Figure 2 is only included to show the approximate boundary of the bubble. Thus, even though the filaments are not parallel to the edge of the superbubble, we suggest that the magnetic field in this region may experience increased compression in a direction toward the Galactic plane (i.e., near the top of Figure 2). If the explosion occurred in a magnetic field with enhanced compression, it may explain the unusual appearance. An association would imply a distance of about 400 pc and a size of ~ 20 pc, which is somewhat small for an old SNR. For a single SNR we can assume an upper limit for a physical diameter of about 100 pc, which gives an upper limit on the distance of 2 kpc.

The spectral index would be useful to confirm this scenario since we expect SNRs to have a spectral index of $\alpha = -0.5 \pm 0.2$ (Reynolds et al. 2012). However, the 160 MHz bandwidth of the GALFACTS data is insufficient for a reliable in-band measurement. We also attempted to measure a spectral index from archival radio data, including 70–231 MHz data from the GaLactic and Extragalactic All-sky MWA Survey (Wayth et al. 2015), 74 MHz Very Large Array Low-frequency Sky Survey (Cohen et al. 2007), the Giant Metrewave Radio Telescope 150 MHz All-sky Radio Survey: First Alternative Data Release (Intema et al. 2017), 2.7 GHz data from the Effelsberg telescope (Reich et al. 1984), and 4.8 GHz data from the Urumqi telescope (Gao et al. 2010). We were unable to get an estimate or even any useful constraints on the spectral index given the faintness of these filaments, artifacts due to the Crab Nebula, and contamination from compact objects in the low-resolution data. Future broader band data with higher resolution are needed to make a spectral index measurement.

4.2. Bow Shock?

Given the suggestive shape, we explore the possibility that G182.5–4.0 is a bow shock nebula. Bow shocks have been observed around neutron stars, in addition to being seen around other massive stars (Ocker et al. 2021). Examples of such objects include the Guitar Nebula, which is associated with PSR B2224+65 (Ocker et al. 2021), and G359.23–0.82, associated with PSR J1747–2958 (Gaensler et al. 2004). In these cases, the bow shock is revealed by high-resolution, multiwavelength observations (including X-rays, radio, and $H\alpha$) in the immediate vicinity of the pulsar/the pulsar wind nebulae (PWN). These objects all have much smaller angular scale than G182.5–4.0, with lengths on the order of a few arcminutes as opposed to several degrees, and the observations show the tip of the bow shock along with a central tail. In the case of the Guitar Nebula, a more extended $H\alpha$ nebula is also revealed. Models of PWN bow shocks (e.g., Gaensler et al. 2004; Petrov et al. 2020)

¹⁹ We note that the highest values of the $H\alpha$ emission are in fact located in the top-right corner, and the corresponding ϕ_{peak} values in this location are quite small. This location corresponds to the known SNR called S147, which is located at a further distance of 1.2 kpc (Green 2019). As noted in the text, Faraday rotation is proportional to a complicated integrated product, and thus, depending on the magnetic field geometry and path lengths, values of high electron density do not always correspond to high Faraday depths.

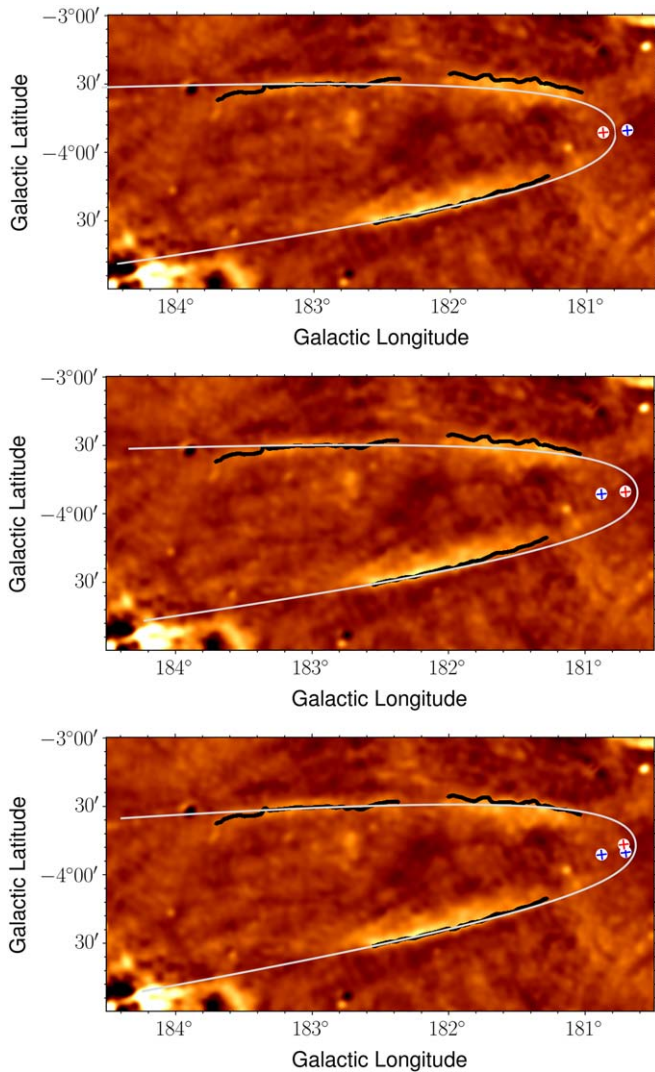


Figure 9. Top panel: Best-fit bow shock model (gray line), with the origin (pulsar position) fixed at the location of the X-ray source, 1RXS J053300.7+260827 (shown with a red cross). The black lines are a series of points defined by a data contour with a level of 0.01 K. The fitted value of $R_0 = 321''$ and the fitted rotation of the model is 5° counterclockwise. The blue cross shows the position of 1RXS J053239.0+261747. The model is shown overlaid on the DRAO polarized intensity image. Middle panel: Same as the top panel, but for the origin (pulsar position) fixed at the location of the X-ray source, 1RXS J053239.0+261747 (shown with a red cross). The fitted value of $R_0 = 310''$ and the fitted rotation of the model is 5° counterclockwise. Bottom panel: Same as the top panel, but without fixing the pulsar position. The best-fit position (shown with a red cross) has R.A. = 5:32:54.5, decl. = +26:18:55, with $R_0 = 313''$ and the fitted rotation of 7° counterclockwise.

show a central PWN with a tail surrounded by a region of shocked ISM that fans out with a larger opening angle. To our knowledge, an example of such an extended bow shock nebula without an associated pulsar has never been found.

We search for X-ray sources near the intersection point of the two filaments (i.e., what would be the tip of the bow shock) and we find two unidentified ROSAT X-ray sources: 1RXS J053239.0+261747 and 1RXS J053300.7+260827 (see Figure 9). These are found in the ROSAT All Sky Survey with a shallow exposure and only a few counts, making it difficult to draw any conclusions from these sources.

As follow-up, we obtained a 7255 s exposure, observed on 2022 September 7, with the Swift spacecraft (Target ID 15319), including imaging with the X-ray Telescope (XRT) and the

Ultraviolet/Optical Telescope (UVOT). While these data, shown in Figure 10, still have only tens of counts, making detailed analysis challenging, we are able to use them to provide much better localization of the ROSAT sources and thus we can determine if there are any known stellar counterparts. For 1RXS J053239.0+261747, HD 244599, a G0-type star (Cannon & Pickering 1993) that is 115.2 ± 0.2 pc away (Gaia Collaboration 2020), is a likely counterpart. For 1RXS J053300.7+260827, there is an M3-type (Reid et al. 2004) star, G98-9, with a distance of 41.90 ± 0.06 pc (Gaia Collaboration 2020). In this case, the cataloged position is well offset from the peak of the X-ray emission. However, from examining the UV image it is clear that the current position of this high-proper-motion star is coincident with the X-ray emission. For this source, there is a second, unidentified UV component (magenta circle in the bottom panel of Figure 10) that is offset by $10''$ from the X-ray peak. It is highly unlikely that the bow shock could be produced by a M- or G-type star, however there remains the possibility that an unseen binary companion is present, perhaps a massive star that produced the bow shock before exploding as a SN. However, it is more likely that the bow shock is unrelated to these sources. Further X-ray follow-up, including a spectral analysis, is needed to assess whether the observed X-ray emission is consistent with emission from the stellar counterpart.

In the case of a bow shock, a star would need to traverse the 3° length of the object since the SN explosion occurred. Assuming a maximum lifetime of 100,000 yr, the minimum speed for such a star is 108 mas yr^{-1} (about 210 km s^{-1} at 400 pc distance). We searched Gaia DR2 data (Gaia Collaboration et al. 2018) but we were unable to locate a star with a fast enough velocity that is also moving in an appropriate direction.

We fit our data with the analytic form of a bow shock (Wilkin 1996),

$$R(\phi) = R_0 \sqrt{3(1 - \phi/\tan \phi)} / \sin \phi, \quad (4)$$

to find the “standoff” distance, R_0 . This gives the opening angle of the shell and the position of the origin, which is the location of the pulsar, and also sets the length scale for the shell. $R(\phi)$ is the distance from the pulsar to the edge of the bow shock and ϕ is the angle between the origin (e.g., pulsar) and the corresponding point on the shock. In order to fit our data, we define a set of points using a contour at a level of 0.01 K, which traces the outer perimeter of the shock (shown as black points in Figure 9). We fit these points for the parameter R_0 , in angular distance units, using $1''$ increments and a least-squares fitting approach. We perform the fits over the range $-170^\circ < \phi < 170^\circ$ in two ways: first by fixing the pulsar position (origin) at the position of each of the ROSAT X-ray sources, and second by allowing the position of the origin to freely vary (in 1 pixel increments, where 1 pixel = $18''$). We also allow the image to freely rotate in 1° increments to find the best-fit rotation angle, θ .

The best fits are shown in Figure 9, with an overall best-fit pulsar position of R.A. = 5:32:54.5 s, decl. = +26:18:55, with $R_0 = 313'' \pm 1''$ and $\theta = 7^\circ \pm 0.5^\circ$. The X-ray source 1RXS J053239.0+261747 is about $3/6$ from the best-fit position.

If we assume a distance equal to that of the Orion-Eridanus superbubble (≈ 400 pc), then $R_0 = 0.6$ pc. This value of R_0 is large compared to many known bow shocks (Gaensler et al. 2004), but it is in excellent agreement with the value found for the Vela X1 bow shock where $R_0 = 0.57$ pc (Gvaramadze et al.

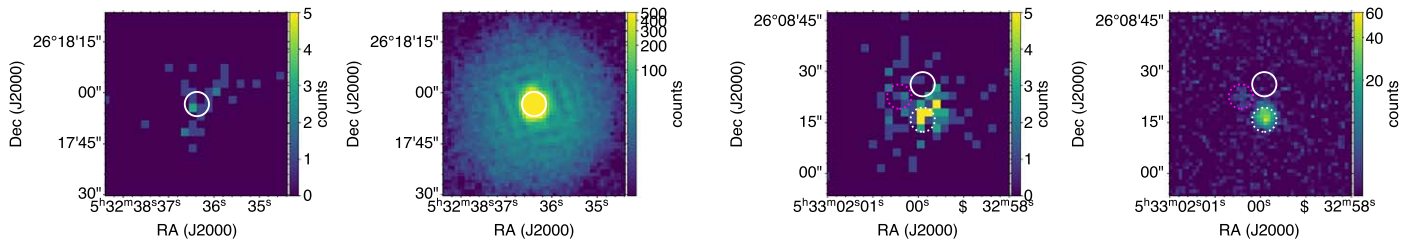


Figure 10. Swift spacecraft images of 1RXS J053239.0+261747 (top) and 1RXS J053300.7+260827 (bottom) including X-ray XRT image (left) and UV UVOT images (right). The white circle in all panels indicates the J2000 catalog coordinates for the stars HD 244599 (top) and G98-9 (bottom). The dotted circles in the bottom panel are drawn centered on the sources seen in the Swift UVOT image. The white dotted circle in the bottom panel is the presumed current location of the high-proper-motion star G98-9. There is a second, unidentified UV component in the bottom-right panel (magenta circle) that is offset by $\sim 10''$ from the X-ray peak.

2018). In that case the distance is around 2 kpc, making the angular size five times smaller, and the nebula is only detected much closer to the pulsar, within $-90^\circ \lesssim \phi \lesssim 90^\circ$. Using the MeerKAT telescope, van den Eijnden et al. (2022) report 1.3 GHz radio emission from the head of this bow shock, which also has an associated $H\alpha$ component. Radio emission has only been observed around a few bow shock nebulae. At this distance the length of the shell is ≈ 19 pc, which is quite long, but it is about the same distance as another known bow shock nebula, the Mouse, which has a length of ≈ 17 pc (assuming a distance of 5 kpc; Gaensler et al. 2004).

The lack of central emission in G182.5–4.0 and the possibility of a large physical size suggests that if it is a bow shock, it is in a different, most likely later, evolutionary stage from the other examples of this type. The very strong evidence connecting the filaments of G182.5–4.0 to the surrounding Galactic ISM implies that its morphology has been shaped by the ambient Galactic magnetic field. If the bow shock scenario is correct, this would be the first time that such a connection has been shown.

There is also the possibility of a hybrid scenario, where both an old SNR and a bow shock nebula are at play. In this case, the radio emission would arise from an old SNR rejuvenated by the relativistic wind of a fast-moving pulsar at the stage of leaving its SNR shell. Such a scenario has been observed from the old SNR CTB 80, characterized by long radio ridges intersecting at the pulsar’s location where a compact bow shock nebula has been also detected (Safi-Harb et al. 1995; Castelletti et al. 2003).

As discussed in the previous section, a spectral index is a useful diagnostic to distinguish a bow shock from the SNR scenario since a bow shock is expected to have a relatively flat spectral index of $-0.3 \lesssim \alpha \lesssim 0$ (Gaensler & Slane 2006). Follow-up observations are needed to measure the spectral index; however, the spectral index measurements to which we are referring have been made in a different part of the bow shock, and it is not clear that this flat spectral index would apply to this extended, shocked ISM structure that we observe. Follow-up X-ray observations at the location of the possible pulsar are crucial to determine their nature and either confirm or rule out the bow shock scenario.

4.3. A Relic Fragment Related to Multiple SN Explosions?

The Orion-Eridanus superbubble is located below the Galactic plane at a distance of ~ 400 pc, and, with a diameter of ~ 300 pc, is thought to have been created by winds or SNe from the Orion OB association (Ochsendorf et al. 2015). Its expansion toward the Galactic plane may be providing additional compression to the Galactic magnetic field in this

region. This may be a factor that is influencing the morphology of the filaments in the two scenarios (SNR or bow shock) already discussed. But a third scenario, that G182.5–4.0 is a fragment in the ISM left over from repeated compression and excitation from successive SN explosions within the superbubble, is also a possibility. If the relic fragment scenario is true, we should expect to find more isolated, nonthermal radio filaments as radio surveys improve in sensitivity and resolution.

5. Conclusions

We have presented the properties of the newly discovered radio filamentary structure that we call G182.5–4.0. We have considered several possible scenarios that could explain this structure, including an old SNR, a bow shock nebula from a neutron star, or a relic fragment left over from one or more very old SN explosions. Given that there is evidence supporting both the old SNR and bow shock scenarios, we consider that G182.5–4.0 is likely a hybrid-type object where we are seeing an old SNR that may be lit up by the wind of a fast pulsar, and that this is a relatively nearby object located in an unusual environment that has been highly compressed by the Orion-Eridanus superbubble.

We find the filaments are oriented at $89^\circ \pm 3^\circ$ (northern filament), and $104^\circ \pm 3^\circ$ (southern filament). Starlight polarization shows consistent orientations for a wide range of distances. Using the RHT technique, we show that HI at a velocity of -8.88 km s $^{-1}$ has an orientation consistent with the Stokes I emission.

We use 3D RM synthesis on the GALFACTS data to measure $F(\phi_{\text{peak}})$, ϕ_{peak} , and χ_{src} near G182.5–4.0. The Faraday rotation appears to have a peak magnitude in close vicinity to G182.5–4.0. Through comparison with $H\alpha$, we conclude that these high negative Faraday depth values are most likely due to a foreground thermal electron cloud.

We make the following conclusions:

1. G182.5–4.0 is polarized, with a high linear polarized fraction of $40^{+30}_{-20}\%$. This indicates that the origin of the emission is synchrotron radiation, which implies the presence of relativistic cosmic ray electrons in a magnetic field.
2. The radial profile of the filaments are consistent with a SN explosion that was centrally located between the two filaments.
3. From its straight morphology and high polarized fraction, the magnetic field of G182.5–4.0 must be highly compressed and not dominated by turbulence.

4. Given that we consistently find $\phi_{\text{peak}} < 0$ over a large spatial area, on average, the magnetic field must be directed away from the observer toward this LOS.
5. The filaments are coincident with an edge of the Orion-Eridanus superbubble, which could be responsible for the high compression of the Galactic magnetic field toward the Galactic plane in this region. An association would imply a distance of ~ 400 pc.
6. The shape of the filaments are well fit by a typical bow shock shape, with $R_0 = 313'' \pm 1''$. At a distance of 400 pc, $R_0 = 0.6$ pc.
7. We have established that there is a strong connection between the orientation of G182.5–4.0 and the Galactic magnetic field direction in the surrounding region. This is supported by starlight polarization and neutral hydrogen. In the case of an association with the Orion-Eridanus superbubble, a connection is not surprising as we would expect the compression in the bubble wall to effect all of the magnetic field tracers in a similar manner. However, such a connection is unexpected in the case of a bow shock nebula since we expect the shape to be dominated by the velocity of the originating object (i.e., star or pulsar). Thus, if G182.5–4.0 is a bow shock, then either the magnetic field alignment is purely coincidental or there is a link between the kinematics and the magnetic field orientation.










Targeted observations from the Effelsberg telescope or the Very Large Array would allow for more detailed analysis of the morphology and an accurate spectral index measurement. Spectral index is an important clue to provide additional evidence to confirm the true origin of this object. Further follow-up X-ray observations of the compact sources near the tip of G182.5–4.0 are necessary to confirm or exclude the bow shock scenario.

These filaments may represent some new class of objects, either as some hybrid between a SNR and a bow shock nebula and/or the result of repeated compression in the ISM due to successive SN explosions. Filaments such as these may be commonplace in the Galaxy. Studying and locating distances to such filaments could become an important tool to help trace the Galactic magnetic field and construct a true 3D picture of it. Future higher-resolution and wide-bandwidth radio observations such as those from the LOFAR Two Meter Sky Survey (Shimwell et al. 2019, 2022), the Australian Square Kilometer Array Pathfinder Evolutionary Map of the Universe survey (Norris et al. 2011), and polarization observations from the Polarization Sky Survey of the Universe’s magnetism (Gaensler et al. 2010) could help detect other similar filaments.

We acknowledge and thank the referee for their helpful comments that improved this manuscript. This research has made use of the NASA Astrophysics Data System (ADS). This research made use of Astropy,²⁰ a community-developed core Python package for Astronomy. We acknowledge the use of NASA’s SkyView facility, located at the NASA Goddard Space Flight Center. This research made use of Montage. It is funded by the National Science Foundation under grant No. ACI-1440620, and was previously funded by the National Aeronautics and Space Administration’s Earth Science Technology Office, Computation Technologies Project, under

Cooperative Agreement Number NCC5-626 between NASA and the California Institute of Technology. This research made use of APLpy, an open-source plotting package for Python (Robitaille & Bressert 2012; Robitaille 2019). The Dunlap Institute is funded through an endowment established by the David Dunlap family and the University of Toronto. J.L.W. and B.M.G. acknowledge the support of the Natural Sciences and Engineering Research Council of Canada (NSERC) through grant No. RGPIN-2015-05948, and of the Canada Research Chairs program. S.S.H. acknowledges support from NSERC through the Discovery Grants and the Canada Research Chairs programs and by the Canadian Space Agency. J.L.C. acknowledges support from the Ontario Graduate Student Scholarship. J.M.S. acknowledges the support of the Natural Sciences and Engineering Research Council of Canada (NSERC), 2019-04848. The DRAO Synthesis Telescope is operated by the National Research Council Canada as a national facility. This paper makes use of data obtained as part of the IGAPS merger of the IPHAS and UVEX surveys carried out at the Isaac Newton Telescope (INT). The INT is operated on the island of La Palma by the Isaac Newton Group in the Spanish Observatorio del Roque de los Muchachos of the Instituto de Astrofísica de Canarias. All IGAPS data were processed by the Cambridge Astronomical Survey Unit, at the Institute of Astronomy in Cambridge. The uniformly calibrated bandmerged IGAPS catalog was assembled using the high-performance computing cluster via the Centre for Astrophysics Research, University of Hertfordshire.

ORCID iDs

J. L. West  <https://orcid.org/0000-0001-7722-8458>
 J. L. Campbell  <https://orcid.org/0000-0002-2511-5256>
 R. Kothes  <https://orcid.org/0000-0001-5953-0100>
 S. Safi-Harb  <https://orcid.org/0000-0001-6189-7665>
 J. M. Stil  <https://orcid.org/0000-0003-2623-2064>
 A. R. Taylor  <https://orcid.org/0000-0001-9885-0676>
 T. Foster  <https://orcid.org/0000-0002-3189-4882>
 B. M. Gaensler  <https://orcid.org/0000-0002-3382-9558>
 S. J. Gibson  <https://orcid.org/0000-0002-1495-760X>
 R. Ricci  <https://orcid.org/0000-0003-4631-1528>

References

- Barentsen, G., Farnhill, H. J., Drew, J. E., et al. 2014, *MNRAS*, **444**, 3230
 Beck, R. 2015, *A&ARv*, **24**, 4
 Bracco, A., Benjamin, R. A., Alves, M. I. R., et al. 2020, *A&A*, **636**, L8
 Brentjens, M. A., & de Bruyn, A. G. 2005, *A&A*, **441**, 1217
 Burton, W. B. 1972, *A&A*, **19**, 51
 Cabral, B., & Leedom, L. C. 1993, in Proc. 20th Annual Conf. on Computer Graphics and Interactive Techniques, SIGGRAPH '93 (New York: ACM), 263
 Campbell, J. L., Clark, S. E., Gaensler, B. M., et al. 2022, *ApJ*, **927**, 49
 Cannon, A. J., & Pickering, E. C. 1993, VizieR Online Data 135A/135A, <http://vizier.cfa.harvard.edu/viz-bin/VizieR?source=III/135A>
 Castelletti, G., Dubner, G., Golap, K., et al. 2003, *AJ*, **126**, 2114
 Caswell, J. L. 1977, *PASA*, **3**, 130
 Clark, S. E., Peek, J. E. G., & Putman, M. E. 2014, *ApJ*, **789**, 82
 Cohen, A. S., Lane, W. M., Cotton, W. D., et al. 2007, *AJ*, **134**, 1245
 De Vries, M., & Romani, R. W. 2022, *ApJ*, **928**, 39
 Dickel, J. R., & Milne, D. K. 1976, *AuJPh*, **29**, 435
 Drew, J. E., Greimel, R., Irwin, M. J., et al. 2005, *MNRAS*, **362**, 753
 Fesen, R. A., Drechsler, M., Weil, K. E., et al. 2021, *ApJ*, **920**, 90
 Foster, T., & Cooper, B. 2010, in ASP Conf. Ser. 438, The Dynamic Interstellar Medium: A Celebration of the Canadian Galactic Plane Survey, ed. R. Kothes, T. L. Landecker, & A. G. Willis (San Francisco, CA: ASP), 16

²⁰ <http://www.astropy.org>

- Gaensler, B. M. 1998, *ApJ*, **493**, 781
- Gaensler, B. M., Landecker, T. L., Taylor, A. R. & POSSUM Collaboration 2010, *BAAS*, **42**, 515
- Gaensler, B. M., & Slane, P. O. 2006, *ARA&A*, **44**, 17
- Gaensler, B. M., van der Swaluw, E., Camilo, F., et al. 2004, *ApJ*, **616**, 383
- Gaia Collaboration 2020, *VizieR On-line Data Catalog*, I/350, doi:10.26093/cds/vizieR.1350
- Gaia Collaboration, Brown, A. G. A., Vallenari, A., et al. 2018, *A&A*, **616**, A1
- Gao, X. Y., Reich, W., Han, J. L., et al. 2010, *A&A*, **515**, A64
- Green, D. A. 2019, *JApA*, **40**, 36
- Green, S., Mackey, J., Kavanagh, P., et al. 2022, *A&A*, **665**, A35
- Gvaramadze, V. V., Alexashov, D. B., Katushkina, O. A., & Kniazev, A. Y. 2018, *MNRAS*, **474**, 4421
- Haffner, L. M., Reynolds, R. J., Tuftte, S. L., et al. 2003, *ApJS*, **149**, 405
- Heiles, C. 2000, *AJ*, **119**, 923
- Heywood, I., Rammala, I., Camilo, F., et al. 2022, *ApJ*, **925**, 165
- Intema, H. T., Jagannathan, P., Mooley, K. P., & Frail, D. A. 2017, *A&A*, **598**, A78
- Jaffe, T. R., Leahy, J. P., Banday, A. J., et al. 2010, *MNRAS*, **401**, 1013
- Jansson, R., & Farrar, G. R. 2012, *ApJ*, **757**, 14
- Jelić, V., de Bruyn, A. G., Pandey, V. N., et al. 2015, *A&A*, **583**, A137
- Joubaud, T., Grenier, I. A., Ballet, J., & Soler, J. D. 2019, *A&A*, **631**, A52
- Landecker, T. L., Clutton-Brock, M., & Purton, C. R. 1990, *A&A*, **232**, 207
- Landecker, T. L., Dewdney, P. E., Burgess, T. A., et al. 2000, *A&AS*, **145**, 509
- Meng, M.-n., & Sun, X.-h. 2021, *ChA&A*, **45**, 162
- Norris, R. P., Hopkins, A. M., Afonso, J., et al. 2011, *PASA*, **28**, 215
- Ochsendorf, B. B., Brown, A. G. A., Bally, J., & Tielens, A. G. G. M. 2015, *ApJ*, **808**, 111
- Ocker, S. K., Cordes, J. M., Chatterjee, S., & Dolch, T. 2021, *ApJ*, **922**, 233
- Page, L., Hinshaw, G., Komatsu, E., et al. 2007, *ApJS*, **170**, 335
- Parker, E. N. 1992, *ApJ*, **401**, 137
- Petrov, A. E., Bykov, A. M., & Osipov, S. M. 2020, *JPhCS*, **1697**, 012002
- Planck Collaboration, Adam, R., Ade, P. A. R., et al. 2016, *A&A*, **586**, A135
- Purcell, C. R., Van Eck, C. L., West, J., Sun, X. H., & Gaensler, B. M. 2020, *RM-Tools: Rotation Measure (RM) Synthesis and Stokes QU-fitting*, *Astrophysics Source Code Library*, ascl:2005.003
- Reich, W., Fuerst, E., Haslam, C. G. T., Steffen, P., & Reif, K. 1984, *A&AS*, **58**, 197
- Reid, I. N., Cruz, K. L., Allen, P., et al. 2004, *AJ*, **128**, 463
- Reid, M. J., Menten, K. M., Brunthaler, A., et al. 2019, *ApJ*, **885**, 131
- Reynolds, S. P., Gaensler, B. M., & Bocchino, F. 2012, *SSRv*, **166**, 231
- Robitaille, T. 2019, *APLpy v2.0: The Astronomical Plotting Library in Python v.2.0.3*, Zenodo, doi:10.5281/zenodo.2567476
- Robitaille, T., & Bressert, E. 2012, *APLpy: Astronomical Plotting Library in Python*, *Astrophysics Source Code Library*, ascl:1208.017
- Safi-Harb, S., Ogelman, H., & Finley, J. P. 1995, *ApJ*, **439**, 722
- Sedov, L. I. 1959, *Similarity and Dimensional Methods in Mechanics* (Waltham: Academic Press)
- Shimwell, T. W., Hardcastle, M. J., Tasse, C., et al. 2022, *A&A*, **659**, A1
- Shimwell, T. W., Tasse, C., Hardcastle, M. J., et al. 2019, *A&A*, **622**, A1
- Sofue, Y. 2020, *PASJ*, **72**, L4
- Sun, X. H., Reich, W., Waelkens, A., & Enßlin, T. A. 2008, *A&A*, **477**, 573
- Tahani, M., Glover, J., Lupypciw, W., et al. 2022, *A&A*, **660**, L7
- Taylor, A. R., Gibson, S. J., Peracaula, M., et al. 2003, *AJ*, **125**, 3145
- Taylor, A. R., & Salter, C. J. 2010, in *ASP Conf. Ser. 438, The Dynamic Interstellar Medium: A Celebration of the Canadian Galactic Plane Survey*, ed. R. Kothes, T. L. Landecker, & A. G. Willis (San Francisco, CA: ASP), 402
- van den Eijnden, J., Heywood, I., Fender, R., et al. 2022, *MNRAS*, **510**, 515
- Wang, Y., Tuntsov, A., Murphy, T., et al. 2021, *MNRAS*, **502**, 3294
- Wayth, R. B., Lenc, E., Bell, M. E., et al. 2015, *PASA*, **32**, e025
- West, J. L., Landecker, T. L., Gaensler, B. M., Jaffe, T., & Hill, A. S. 2021, *ApJ*, **923**, 58
- West, J. L., Safi-Harb, S., Jaffe, T., et al. 2016, *A&A*, **587**, A148
- Wilkin, F. P. 1996, *ApJL*, **459**, L31
- Yusef-Zadeh, F., Morris, M., & Chance, D. 1984, *Natur*, **310**, 557
- Zaroubi, S., Jelic, V., de Bruyn, A. G., et al. 2015, *MNRAS*, **454**, L46